JOURNAL OF Materials CHEMISTRY

Electronic properties of $ZrTe_3$‡

C. Felser, E. W. Finckh, H. Kleinke,† F. Rocker and W. Tremel*

Institut für Anorganische Chemie und Analytische Chemie, Johannes Gutenberg-Universität, Becher Weg 24, Mainz D-55099, Germany

We present the results of a combined experimental and theoretical study of the electronic structure of $ZrTe_3$. $ZrTe_3$ is a material that undergoes a transition to a charge density wave state at 63 K and displays superconductivity below 2 K. The results of photoemission measurements using synchrotron radiation as well as temperature dependent resistivity and thermopower data allow one to sketch a detailed experimental picture of the electronic structure at the Fermi level. High level TB-LMTO-ASA band structure calculations are used to analyze the bonding situation in $ZrTe_3$ and to relate the physical properties of the crystal to the electronic structure. $ZrTe_3$ is a layered material whose structure is built up from trigonal prismatic $ZrTe_3$ chains with extensive Te—Te interactions perpendicular to the chain direction. These Te—Te interactions lead to wide bands in the direction perpendicular to the chains of trigonal prisms. Frozen phonon calculations indicate that the density of states at the Fermi level and the shape of the Fermi surface are strongly dependent on the Te—Te interprism interactions. The complete computed Fermi surface consists of three independent envelopes: two sheet-like surfaces which are associated with the atoms of the Te_2 group and a cylindrical section, the former one being responsible for the observed charge density wave properties of $ZrTe_3$. The experimental and calculated nesting vectors for the charge density wave are in excellent agreement. A comparison of the band structures of $ZrTe_3$ with those of the isostructural $HfTe_3$ and $ThTe_3$ reveals that $HfTe_3$ should exhibit similar electronic properties as $ZrTe_3$, whereas $ThTe_3$ should be semimetallic. Based on the results of the frozen phonon calculations, we predict a strong pressure dependence of the physical properties of $ZrTe_3$ and $HfTe_3$.

1 Introduction

Cursory consideration of the formula $ZrTe_3$ based on a valence state formalism might lead one to the valence description Zr^{4+}, Te_2^{2-}, and Te^{2-} with semiconducting properties, if two of the Te atoms form a Te_2^{2-} ditelluride group. This would be in agreement with the physical behavior of group 4 chalcogenides MQ_3 (M = Zr, Hf; Q = S, Se),[1] which are semiconducting with band gaps between 1 and 2 eV.[2] In fact, single-crystal resistivity measurements reveal that $ZrTe_3$ is an anisotropic metal[3,4] with a resistivity anomaly at 63 K. In view of the crystal structure which contains trigonal-prismatic MQ_3 chains, it was assumed that, as in other MQ_3 compounds such as $NbSe_3$,[5] which are typical d-band metals, the electrical transport properties are associated with the regularly spaced metal atoms along the trigonal-prism chains.[6] However, subsequent studies have revealed that the unusual physical properties primarily affect the conductivity components perpendicular to the chain direction.[3,4] An electron diffraction study has indicated the presence of a charge density wave (CDW) and has yielded the superlattice vector.[7] Furthermore, $ZrTe_3$ becomes superconducting below 2 K with superconducting filaments spaced at a distance of 4 nm parallel to the *a* axis.[8]

The electronic origin of the CDW has been the subject of an electronic band study at the extended Hückel level by Canadell *et al.*[9] but these results became obsolete when it turned out later that the crystal structure on which these calculations were based[1d] was in error and had to be revised.[10] Finally, we were intrigued by other features of the group 4 tellurides: (i) What is the reason for the 'counterintuitive' electronic transport properties in $ZrTe_3$? Are they predominantly due to metal or non-metal states? (ii) $ZrTe_3$ is particularly interesting in that it exhibits the coexistence of superconductivity and a CDW state. What are the responsible electronic factors? (iii) Owing to weak Te—Te interactions in $ZrTe_3$, its physical properties should be strongly pressure-dependent as observed for $NbSe_3$.[11] What are the effects on the CDW and on T_C under pressure? (iv) As other layered materials, group 4 tritellurides are susceptible to ion intercalation, and their properties may be varied within a certain range in a systematic fashion.[12,13] (v) Finally, we are generally interested in why compounds adopt the structures they have and how their physical properties are related to their crystal and electronic structures, the eventual goal being able to predict the structures and properties of new materials. This contribution is concerned with the electronic structures of the group 4 tellurides.

2 Experimental details

2.1 Sample preparation and characterization

$ZrTe_3$ was prepared following a procedure reported by Furuseth and Fjellvag.[1,10] The powders of Zr (99.9%, Heraeus) and Te (99.8%, Aldrich) were ground together and loaded with I_2 as a chemical transport agent (2 mg/ml ampoule volume) into quartz tubes (approx. 150 mm length, 10 mm i.d.) that were then evacuated and reacted in a temperature gradient from 700 to 650 °C. $ZrTe_3$ grows in the form of shiny metallic plates with dimensions of up to 5×20 mm^2. Several platelets were examined by energy dispersive X-ray analysis.

Room temperature single-crystal and powder diffraction on the samples of $ZrTe_3$ prepared as described here confirm the revised structure of Furuseth *et al.*[10]

2.2 Electronic transport properties

Single-crystal conductivities were measured using a dc four probe technique. Electrode connections to the crystals were made with the use of 100 μm gold wires and indium solder. The thermoelectric properties of $ZrTe_3$ were probed parallel to the crystallographic *a* and *b* axes. Measurements along *c* were not attempted due to the thin platelike crystal shape. For thermopower measurements, a temperature gradient was generated by a Peltier element and detected by a chromel/CuFe

†Presently at the Fachbereich Chemie, Philipps-Universität Marburg, Hans-Meerwein-Straße, D-35043 Marburg, Germany.
‡Dedicated to the memory of Prof. Jean Rouxel.

(0.15%) thermocouple parallel to the sample. The sample was contacted to two silver wires (99.995%, Alfa) by silver conductive paint. The temperature was varied from 300 K to 20 K and back at increments of 5 K. At each temperature eight different gradients in the range $\Delta T = \pm 0.5$ K were applied and the resulting voltage was detected. The Seebeck coefficient was calculated from the slope $dV/d(\Delta T)$ and corrected in regard to the contributions of the silver wire.

2.3 Photoemission

Compact pellets were sintered in quartz ampoules under an argon atmosphere. In the measurement chamber, the pellets were scraped *in situ* at a base pressure better than 10^{-9} bar in order to reduce surface contamination. If contamination was observed during the measurement, the pellets were rescraped. The photoemission measurements were performed at BESSY (Berliner Elektronenspeicherring Gesellschaft für Synchrotron Strahlung mbH) with the TGM3 monochromator in the energy range between 100 eV and 170 eV and a resolution of 0.9 eV, and at the PGM3 monochromator at 70 eV and 100 eV with a resolution of 0.5 eV. The total resolution and the Fermi level were determined by measuring the Fermi cutoff of palladium. Temperature dependent measurements were performed by cooling the samples with liquid nitrogen. A special experimental setup with a large reservoir of liquid nitrogen ensured temperatures of less than 80 K close to the sample. The temperature was monitored using a Ni–Cr/Ni thermocouple.

2.4 Computational details

Band structure calculations based on the structural parameters given in ref. 10 were performed at the extended Hückel[14] level (using the EHMACC software[15]). First-principles self-consistent local density approximation (LDA)[16] calculations of the electronic structure were performed using the LMTO-ASA method.[17] A detailed description of the LMTO-ASA method, including its application to the electronic structure of compounds, has been given elsewhere.[18,19] All *k*-space integrations were performed using the tetrahedron method using 213 irreducible *k*-points in the monoclinic Brillouin zone (BZ). The BZ is as described in ref. 20, where the symmetry points and lines are given in fractions of the reciprocal lattice vectors and labeled in accordance with the standard notation. The choice of the directions depends on the special features of the structure. The one-dimensional Te(2)—Te(3) chains (parallel to the crystallographic *a* direction) correspond to the C (0,1/2,1/2)–E (−1/2,1/2,1/2) and the A (−1/2,1/2,0)–Y (0,1/2,0) directions in reciprocal space, the directions to perpendicular C–E and A–Y correspond to E–D (−1/2,0,1/2) and B (−1/2,0,0)–A in reciprocal space. The main axis of the trigonal prism is directed along the crystallographic *b* direction and corresponds to Γ (0,0,0)–Y in the BZ. The direction perpendicular to the $ZrTe_3$ layers is represented by Γ–Z. The basis set consists of s, p and d orbitals for Zr, and s and p orbitals for Te. The positions of the empty spheres were calculated by an automatic procedure developed by Krier *et al.*[21] In order to study the bonding situation in the vicinity of the Fermi level two new tools of the LMTO program package were used. The orbital character of the bands can easily be visualized with the aid of the so-called fat band representation,[22] where each band is plotted with a width weighted by the charge matrix element of the relevant orbital. The second tool is the so-called COHP (crystal orbital Hamiltonian population),[23] a density of states weighted by the corresponding elements of the Hamiltonian matrix analogous to the COOP (crystal orbital overlap population), an overlap population weighted density of states, which was introduced by Hoffmann and coworkers.[24] Both COHP and COOP indicate in a graphical fashion whether a specific orbital interaction is bonding or antibonding.

3 Results and Discussion

3.1 Crystal structure

Similar to the structures of the other early transition metal trichalcogenides MQ_3 (M = Ti, Zr, Hf, Th, U, Nb, Ta; Q = S, Se, Te)[1] $ZrTe_3$ has infinite MQ_3 chains parallel to the *b* axis as a basic building block. This is emphasized in Fig. 1. The chains associate in a second dimension along the *a* axis through M–Q interchain contacts that are only slightly longer than those within the prism chains. The monoclinic unit cell which is shown in Fig. 1 contains two such chains which are related by an inversion center. Adjacent chains are shifted with respect to each other by *b*/2 along the *b* direction. As a result, each metal atom acquires two additional chalcogenide neighbors, which leaves the metal in effective eight-coordination. The two-dimensional slabs are weakly interacting in the third dimension along the *c* axis. From another point of view, the Te(2) and Te(3) atoms in the $ZrTe_3$ structure are located at the vertices of a rectangular face which is exposed to the interlayer region. In contrast to the group 4 trisulfides and selenides where the bonding situation and the physical proper-

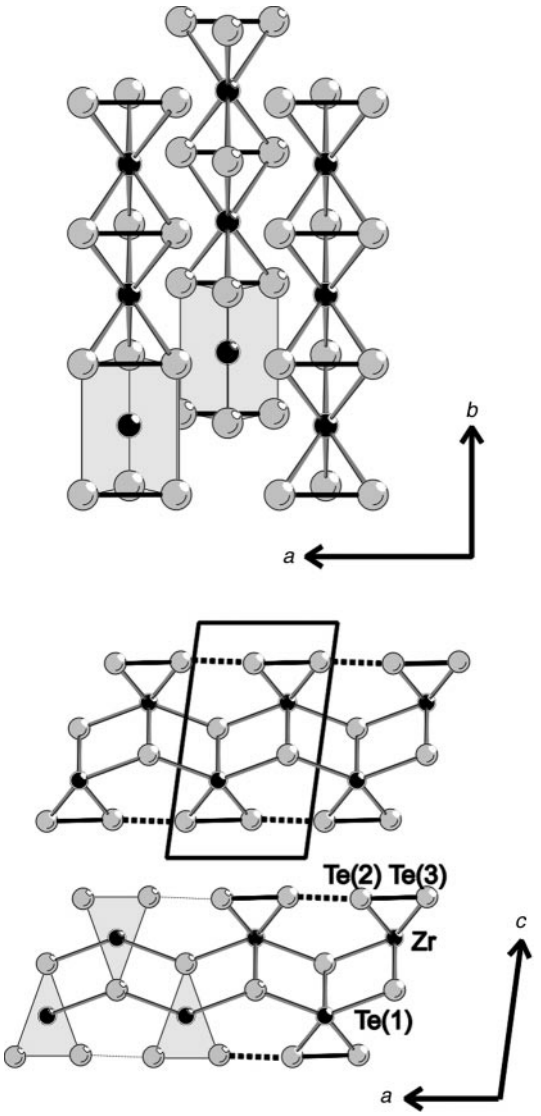

Fig. 1 Crystal structure of $ZrTe_3$. View of the structure along *c* showing the trigonal prism chains. View along *b* emphasizing the layered character of the structure. Important distances: *d*[Zr—Te(1)] 2 × 2.96 Å, *d*[Zr—Te(2)] 2 × 2.94 Å and *d*[Zr—Te(3)] 2 × 2.96 Å (within the prism); *d*[Zr—Te(1)] 3.14 Å and *d*[Zr—Te(1)] 3.16 Å (between prisms); *d*[Te2—Te(3)] 2.79 Å (within the prism); *d*[Te(2)—Te(3)] 3.10 Å (between prisms).

ties may be described unambiguously by electron counting, the situation becomes more complicated for the tritellurides as the Te(2)–Te(3) intrachain distances of approximately 2.80 Å are in agreement with the presence of ditelluride groups, and the Te—Te interchain distances of 3.10 Å along the crystallographic *a* axis clearly indicate some bonding. These separations afford a semicontinuous linear chain of Te atoms extending parallel to the *a* axis.

To begin the analysis of these features we commence with an electron count. Firstly, for the Te(2)–Te(3) chains, if the longer intraprism Te—Te distance is disregarded as a bonding

$(Te_2^{2-})_n$ $(Te)_n$

:Te–Te: :Te–Te: :Te–Te: Te–Te–Te–Te–Te–Te–

1 **2**

interaction, a broken chain, **1**, consisting of Te_2 dimers of composition Te_2^{2-} results. A continuous chain of Te atoms, **2**, a single bond between each atom and six valence electrons per site leads to a representation $(Te)_n$. As Te(1) shows no Te—Te distances within the bonding range, they are counted as Te^{2-}. We can now derive valence descriptions $(Zr^{4+})(Te^{2-})(Te_2^{2-})$ assuming chain **1** or $(Zr^{2+})(Te^{2-})(Te_2)$ assuming chain **2**. As all distances in the Te chain are within the bonding regime, a reasonable valence description lies somewhere between these extremes, *i.e.* the formal valence state of the Zr atoms is somewhere between Zr^{2+} and Zr^{4+}. In order to go from **1** to **2**, the Te chain has to be oxidized and the metal must be reduced. To make this happen, there must be some overlap of the Zr d and Te p states, *i.e.* there must be a band at a low enough energy to accept electrons from the atoms of the Te chain.

3.2 Electronic structure

3.2.1 Te—Te bonding. To model the bonding within the Te—Te chain we use a two-dimensional sheet derived from

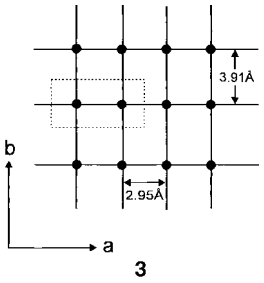

3

the three-dimensional structure. **3** is a rectangular net of Te atoms with lattice constants of 2.95 Å along the *a* axis and 3.91 Å along the *b* axis. The $ZrTe_3$ structure is obtained by inserting the ZrTe(1) portion of the structure between every second pair of adjacent sheets and leaving the interlayer gap unoccupied. The Te slab is a simplified two-dimensional model of the full three-dimensional structure. The band structure of slab **3** is shown in Fig. 2. In consideration of the $ZrTe_3$ structure the unit cell is chosen to contain two Te atoms. The intracellular Te—Te distance in **3** corresponds to the intraprism contact of the $ZrTe_3$ structure; likewise the intercellular Te—Te contact in slab **3** corresponds to the Te—Te separations between adjacent prisms. The band structure of sheet **3** is easily understood. The Te spacing along *a* is considerably shorter than that along *b*. As a result of the large Te—Te separations along *b* the bands along Γ–Y have a much smaller dispersion than along *a*; the width of the p_σ band along *a* is approximately 16 eV, whereas the p_π band exhibits a bandwidth of 3 eV which is comparable to the width of the p_σ bands along *b*.

The π band components along *b* are almost flat and dispersionless. The energy bands of the Te sheet may be derived from those of a one-dimensional Te chain. Given on the left in Fig. 2 are the crystal orbitals of the rectangular net **3** at the zone center; the energy ordering may be understood in a straightforward manner based on the hierarchy of interactions. The π and π* orbitals of the Te chains lead to a classical free-electron type band. The π_y and π_z bands of the Te sheet are not degenerate because there is a weak σ antibonding component in the π_y orbital. For electron counts close to seven electrons per Te atom the σ* band is partially filled, for somewhat lower electron counts close to six a portion of the π* band remains empty. The Fermi level for the Te sheet is between −10 and −9 eV, and metallic properties are expected. The electronic structure resembles that of a typical one-dimensional conductor and, for a half-filled σ band, should be susceptible to a Peierls-type distortion which eventually leads to isolated Te_2^{2-} units.

3.2.2 Band structure. The resulting band structure of $ZrTe_3$ is given in Fig. 3. Since interlayer interactions may be expected to be less significant, the bands are plotted in the layer plane perpendicular to the van der Waals gap; the Te s bands are outside the given energy window. Fig. 3(a) shows the energy bands computed within the extended Hückel approximation, Fig. 3(b) shows the results of a band calculation using the TB-LMTO-ASA method. Te(2)/Te(3) p_x eigenvector contributions are pronounced by the fatband representation. In a qualitative sense, all the essential features of the band structure of the Te layer **3** are preserved in the full $ZrTe_3$ band structure. Along the lines Γ–B and A–Y in Fig. 3(a), the heavy lines refer to the Te p_σ bands; since the unit cell contains two Te layers there are twice as many bands corresponding to the symmetric and antisymmetric combinations. The symmetry present in the idealized Te model structure is lost in the real $ZrTe_3$ structure; therefore no degeneracies are observed at B. The bandwidth of 16 eV for the Te p_σ bands is comparable to that observed for the Te model structure. Eight Te p bands are located in the energy window between −16 and −12 eV. For a total of 44 electrons per unit cell the lowest 22 bands [6 Te s, 6 Te(1) p, 8 Te(2)/Te(3) p_π and 2 Te(2)/Te(3) p_σ bands] must be filled. Above the Fermi level, the bands of $ZrTe_3$ have mostly Zr d-orbital character, their detailed nature being determined by the local crystal field. The coordination environment of the Zr atoms is a bicapped trigonal prism. The corresponding crystal field splitting follows a one below four pattern.[25] The lowest orbital of the metal d set is the d_{y^2} orbital which is directed along the main axis of the trigonal prism around the metal atom. The crystal field splitting is small, and, at the zone center, the remnant of the metal d block manifold is located approximately 3 eV above the d_{y^2} bands. As in the band structure of the Te sheet, the Fermi level for the full $ZrTe_3$ band structure is located in the middle of the Te p_σ band and cuts this band along the line B–A.

In the EH approximation the position of the Fermi level is parameter dependent. Since the Fermi level for $ZrTe_3$ is situated in the middle of three bands with low dispersion, it is immediately apparent that the shape of the Fermi surface will be strongly determined by the position of the Fermi level. In order to achieve a higher numerical accuracy for the determination of the nesting vectors, we have performed *ab-initio* band structure calculations using the TB-LMTO-ASA method. The resulting self-consistent LMTO band structure is presented in Fig. 3(b) side by side with the extended Hückel band structure. The general features of the LMTO band structure are compatible with those of the extended Hückel calculation. In particular, the Te(2)/Te(3) centered p_x bands are situated in the vicinity of E_F along B–A. However, a closer look indicates that the position of E_F differs as now three bands (nos. 22–24) instead of two (nos. 21 and 22 using the EH method) cut the Fermi level. Using the fat-band representations we will demonstrate that the orbital pictures which we have used to illustrate

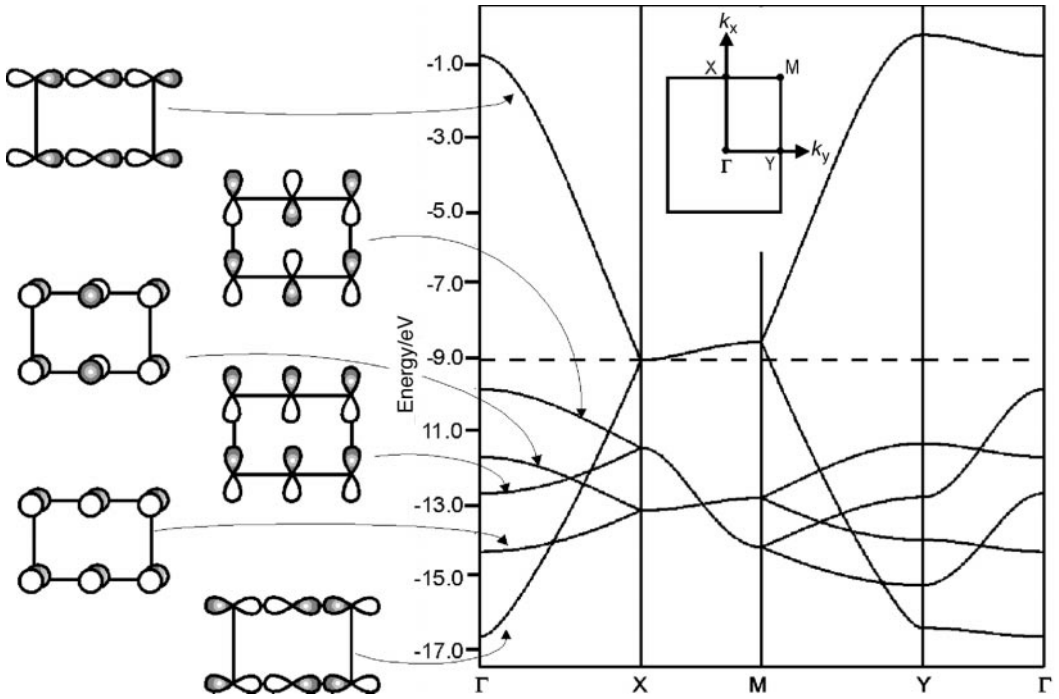

Fig. 2 Band structure for a two-dimensional Te array, as drawn in **3**

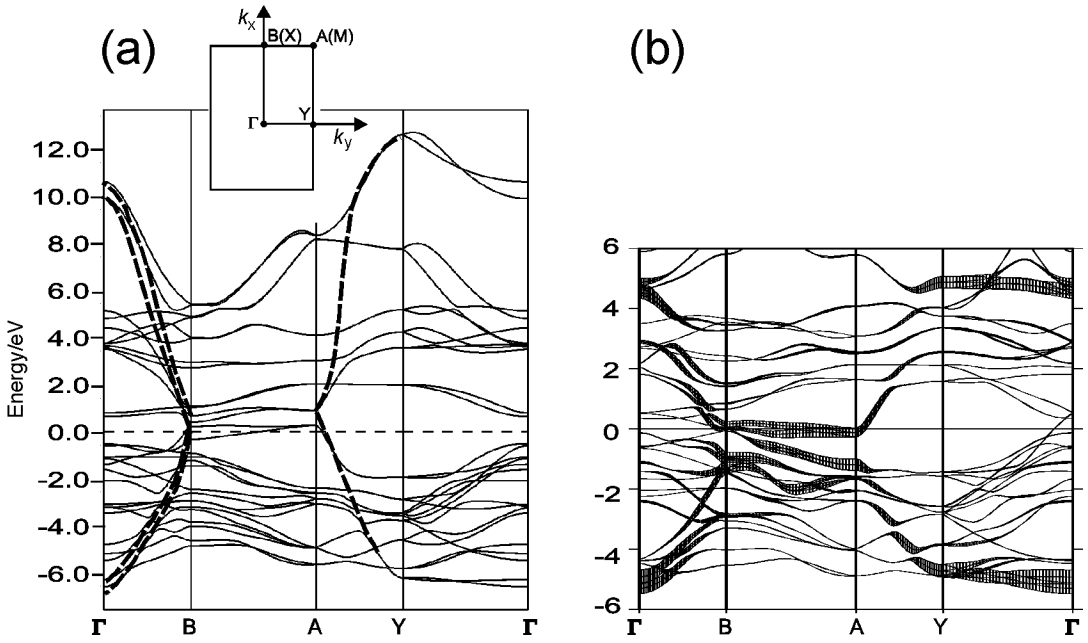

Fig. 3 $ZrTe_3$ band structures along the lines Γ–B–A–Z–Γ in the a^*, b^* plane using (a) the extended Hückel and (b) the TB-LMTO-ASA method, in a p_x fatband projection

the $ZrTe_3$ band structure in the previous section are valid for the *ab initio* band structure.

In the following sections we show that the physical properties of $ZrTe_3$-type compounds may be related in a straightforward manner to the crystal structure. The band structure in Fig. 3 may be interpreted using the densities of states and their individual atom or orbital contributions, the crystal orbital Hamiltonian population (COHP) as well as the fat-band approach. It is noted from the previous section that the Te(2)/Te(3) centered p_σ bands are dispersive along the symmetry lines Γ–B and Y–A and almost flat along B–A and Γ–Y. Since these bands are responsible for the properties of $ZrTe_3$, we now examine their nature.

3.2.3 Density of states. The total and projected density of states (DOS) calculated for Zr d, and Te(1) and Te(2), are shown in Fig. 4. In analogy to molecular examples, there is a net electron transfer from Te to the metal. The charge transfer is not restricted to the atoms of the Te sheet; in the full $ZrTe_3$ structure there is also a donation of charge from the isolated Te atoms to the metal. In summary, the soft Te—Te interactions and the alternation of the Te—Te intra- and interprism bonding are the result of redox competition[26] *i.e.* a partial electron transfer from Te to the metal. We find a broad peak for the density of states at the Fermi level; this is compatible with the observed metallic properties of $ZrTe_3$ at room temperature. The DOS at E_F is dominated by Te p contributions; the

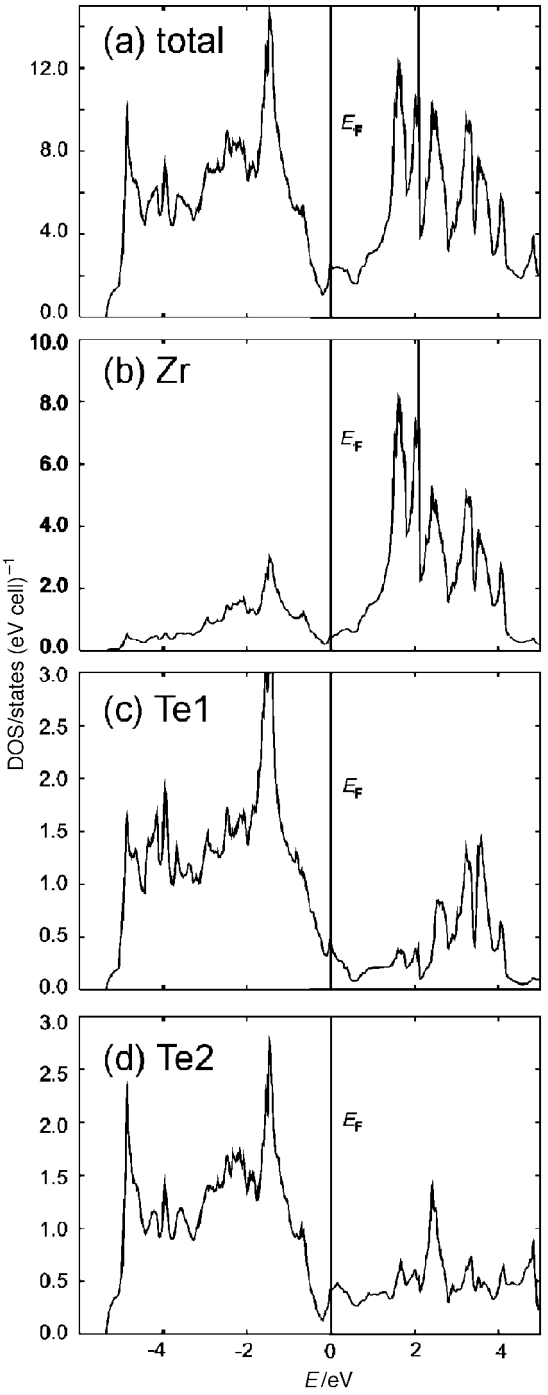

Fig. 4 Total LMTO-ASA density of states for (a) $ZrTe_3$ and the partial DOS of (b) Zr, (c) Te(1) p and (d) Te(2) p. The vertical lines mark the Fermi energy.

contribution of the Zr d states to the valence band increases as the Fermi energy is approached [Fig. 4(b)], and only becomes significant above E_F. There is no significant difference between the DOS contributions of the chemically equivalent Te(2) and Te(3) atoms, therefore only the partial density of Te(2) is shown. Both types of tellurium atoms contribute to the valence band in a similar manner. This is in sharp contrast to the assignment of formal oxidation states, which implies different values for Te(1) and Te(2)/Te(3). Obviously, in the real structure the oxidation states are leveled out, which can be rationalized as a different degree of electron transfer to the metal.

3.2.4 Analysis of the COHP. The COHP plots provide insight into the bonding interactions in $ZrTe_3$. They indicate the bonding and antibonding contribution of the levels in a given energy interval to a specified bond and for a given orbital contribution. We focus on the interactions between the different components of the $ZrTe_3$ structure. The Zr and Te [Te(1) *vs.* Te(2)/Te(3)] interactions may be followed through the DOS contributions in Fig. 4 and the COHP curves in Fig. 5. The corresponding antibonding states are located at the top of the p band above E_F, whereas the bonding interactions at the bottom of the p band are slightly reduced by the s–p mixing. The strongest interactions are within the Te(2)–Te(3) chains. Fig. 5(c)–(e) clearly show the wide and highly dispersed p band: its bottom is Te—Te bonding, the top Te—Te antibonding. The Te—Te intraprism interactions are illustrated in Fig. 5(c), Fig. 5(e) shows the Te—Te interprism interactions. The COHP curves in Fig. 5(c)–(e) display some small but distinct differences: whereas the character of the Te—Te p_σ interactions mediated through the p_x orbitals that are plotted in Fig. 5(d) switches from bonding to antibonding at the Fermi level, the total Te—Te interaction which is displayed in Fig. 5(c) picks up some antibonding character approximately 0.7 eV below E_F which can be attributed to the π antibonding contribution of the p_y and p_z states. In contrast, the Te—Te interprism interactions are much weaker; they are bonding at the bottom of the p band, but their character changes to antibonding in the middle of the p block below the

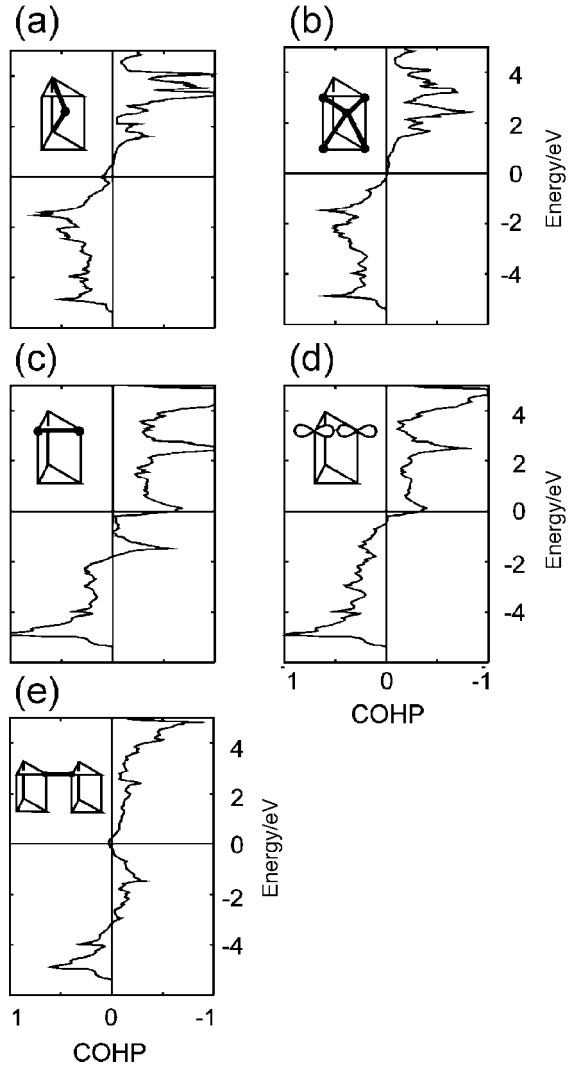

Fig. 5 COHP of (a) the Zr—Te(1) interaction, (b) Zr—Te(2) interaction, (c) Te(2)—Te(3) interaction within the prism, (d) the Te(2) p_x—Te(3) p_x interaction within the prism, and (e) the Te(2)—Te(3) interaction between adjacent prisms.

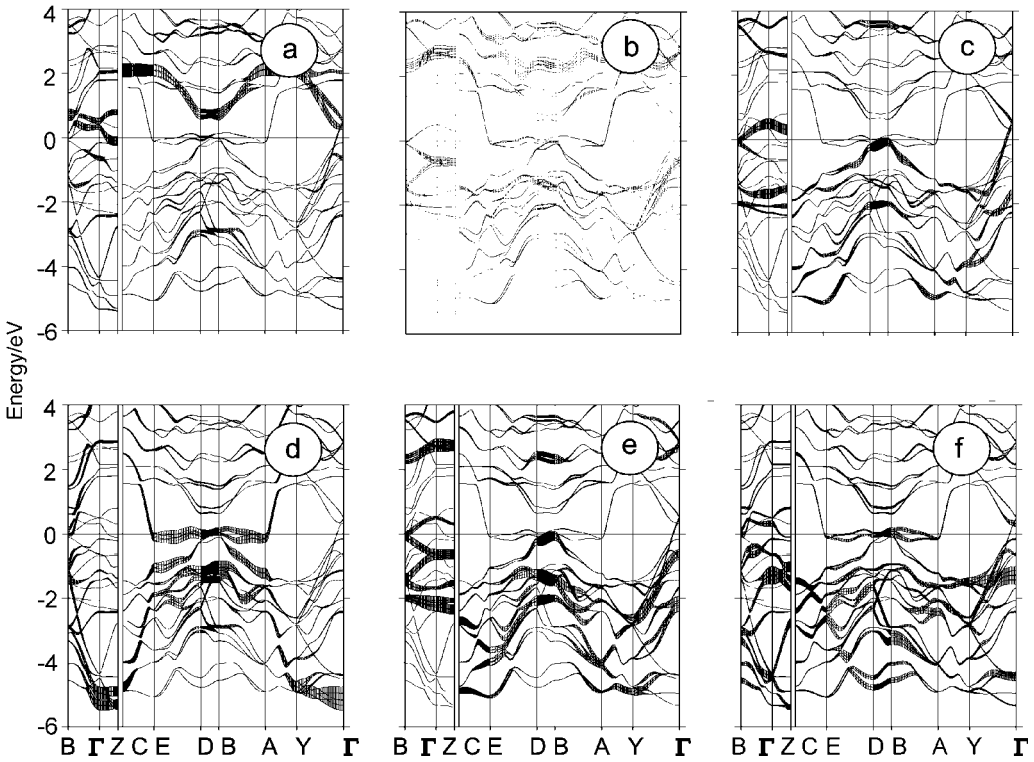

Fig. 6 Fatbands of $ZrTe_3$. (a), (b) show the fatbands projected on the Zr d_{y^2} and d_{xy}, (c) Te(1) p_y, and (d)–(f) Te(2) plus Te(3) p_x, p_y, and p_z. 100% eigenvectors contribution corresponds to 0.25 eV.

Fermi level and finally turns strongly antibonding above the Fermi level.

3.2.5 Fat-bands. Fig. 6 shows a fat-band representation of the important eigenvector contributions to the states at E_F for $ZrTe_3$. The Brillouin zone and the relevant symmetry directions

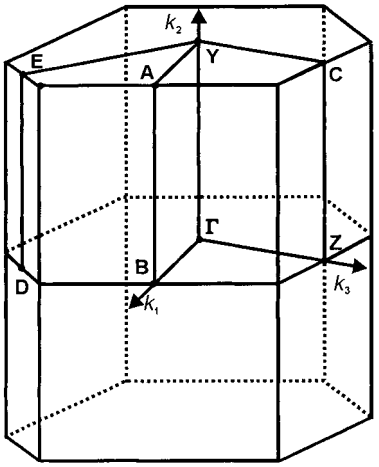

4

are given in **4**. We have computed the energy bands along the directions parallel to the $ZrTe_3$ layer as well as along selected symmetry lines perpendicular. The panels in Fig. 6(a)–(c) give the contributions of two selected zirconium orbitals (d_{y^2}, d_{xy}) and Te(1) p_y. Fig. 6(d)–(f) show the contributions of Te(2)/Te(3) p_x, p_y, and p_z. The eigenvector contribution is represented by the line width, 100% corresponds to 0.5 eV on the energy scale. As expected, the metal centered bands are located above the Fermi level, the only notable exception being the Zr d_{y^2} band [Fig. 6(a)] which crosses E_F along Γ–Z to build an electron pocket around Z. All Zr d states mix into Te bands of suitable symmetry below E_F. One example is illustrated in **5**. The d_{xy} orbitals overlap with π^*_y orbitals of

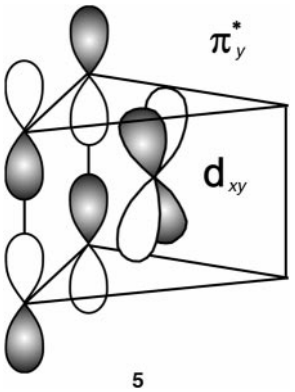

5

the Te_2 units, situated 0.5 eV below E_F at Γ [Fig. 6(b)]. At 3 eV above E_F we find the corresponding contributions of the antibonding Te states [Fig. 6(e)]. It is obvious that bands with a substantial d_{xy} contribution are flat along Γ–Z and parallel directions, but disperse along B–Γ and Y–Γ. The states at the Fermi level have major contributions from the p_x orbitals of Te(2)/Te(3), forming σ* bands [Fig. 6(d)]. One of the σ* bands (no. 23) crosses the Fermi level along E–D and B–A (parallel to Γ–Y); by symmetry, it is degenerate with the second σ* band (no. 24) along the lines C–E and A–Y. The second is situated mostly above E_F along the E–D and the B–A directions. The quasi one-dimensional character of the Te chain is reflected in the large dispersion of these σ* bands along B–Γ, C–E and A–Y; the bandwidth in the absence of several avoided crossings would be approximately 5 eV, with the top of the band at the zone center and the bottom at B. The σ and the σ* bands, which were degenerate at B in the 2D model (Fig. 2), are now separated by an energy of 1 eV [Fig. 6(d)] owing to the non-equal Te—Te bond lengths. The top of the σ band is nearly 1 eV below the Fermi energy at B, the bottom portion being approximately 6 eV below E_F at the zone center.

Similar to their σ* counterparts, the Te σ bands are flat along Γ–Z and other directions perpendicular to the $ZrTe_3$

layer. In the light of the introductory section which focused on interactions between Te(2) and Te(3) which form the rectangular net, it may seem surprising that there is a large p_y contribution of Te(1) to the states in the vicinity of the Fermi level. Furthermore, these bands disperse, in particular along Γ–Y and other lines parallel to b^*. The Fermi level cuts through the Te(1) p_y band (no. 22) along Γ–Y; thus conductive behavior can be expected along b. What is the reason for the dispersive behavior of the bands along this direction? The Te—Te distance of 3.9 Å along b is rather long; but the interaction is strong enough to produce a sizeable dispersion and to push the top of the p_y band above the Fermi level. The nodal properties force these p_y bands to lower energies as one moves along symmetry lines parallel to b^*. Since the p_y bands are almost flat along B–Γ and Γ–Z, their contribution to the states at the Fermi level is substantial.

3.3 Fermi surface and electronic properties

3.3.1 Fermi surface. The Fermi surface (FS) of $ZrTe_3$ is shown in Fig. 7 in a view along c^* (parallel to Γ–Z). The color coding of the plot symbolizes the Fermi velocities: red corresponds to high Fermi velocities, and low Fermi velocities are indicated in blue. Since the Fermi level cuts through three bands, one expects a FS with three branches. As anticipated from the previous section, several branches of the FS of $ZrTe_3$ are open and quasi-planar; in addition, there is a closed portion with a tunnel-like shape along the a^* direction. This is caused by the fact that the Fermi level intersects the Zr d_{y^2} band in the Γ–Z direction and that the Te(1) p_y band drops below E_F along Γ–Y, *i.e.* the tunnel-like portion of the FS is related to the presence of two partially filled bands. A special feature of this section is the pentagonal holes that interpenetrate the cylinder in a direction parallel to c^*. The observed metallic properties of $ZrTe_3$ along the needle axis (*i.e.* the crystallographic b direction) must be related to the spherical character of this inner branch of the FS.

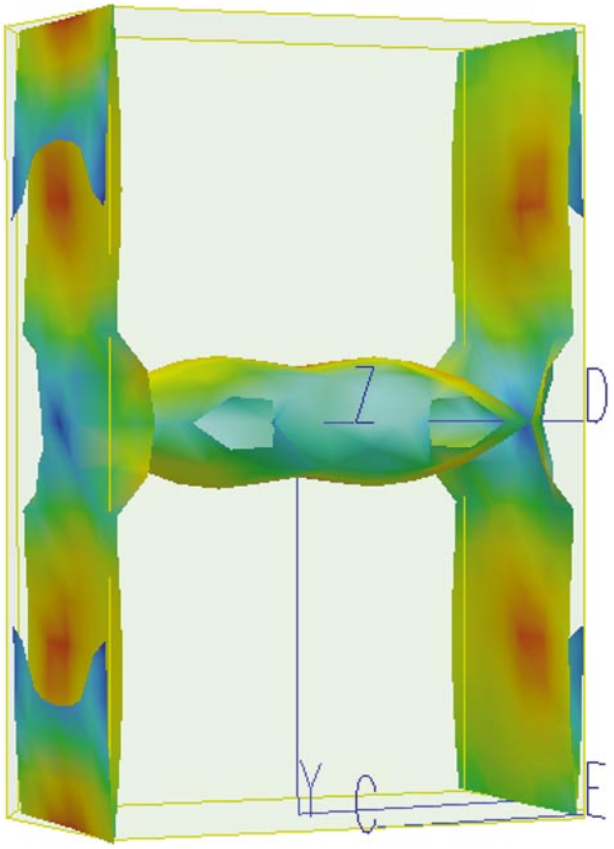

Fig. 7 LMTO-ASA Fermi surface of $ZrTe_3$. Red regions correspond to high dispersion (high Fermi velocity) and blue regions to low dispersion (low Fermi velocity).

The quasi-planar second and third branches of the FS are mainly derived from the linear chains of Te(2)/Te(3) atoms; they consist of planar sheets parallel to the b^* direction that are associated with a pair of bands (no. 23, 24). From Fig. 6(d) it is apparent that these bands have almost pure Te(2)/Te(3) p_x character. Both members of this pair are flat and almost completely filled along E–D–B–A; the lower band which is associated with the second branch of the FS touches the Fermi level close to B. The strong orbital interactions within the Te(2)/Te(3) chains lead to high Fermi velocities as indicated by the red color of the Fermi surface plot within these two branches. The blue color of a small part of this branch near the B point indicates low Fermi velocity and virtually no band dispersion. Near B, the second branch of the FS is undulating rather than flat. We believe this to be a consequence of interlayer interactions.

3.3.2 CDW nesting vector. The resistance anomaly at 63 K was found to be associated with the occurrence of superlattice spots with a vector $q_{exp} = 0.93\,a^* + 0.33\,c^*$, observed by electron diffraction at 50 K.[7] CDW instabilities are a consequence of parallel planar sections of the Fermi surface,[27] and our FS calculation confirms the assignment of the anomaly in $ZrTe_3$ to a CDW transition. The calculated FS sheets are not perfectly parallel, and we approximate the theoretical nesting vector on the basis of simple geometry. The nesting vector is sketched in

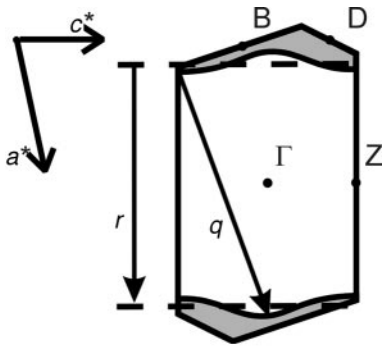

6

6, filled regions of the Brillouin zone at $b^* = 0$ are shaded. The vector connecting the centers of the large pseudo-parallel parts of the FS is given by $r = 0.93a^* - 0.22c^*$, the c^* component only compensating the oblique β^* angle. The undulations near B–D have their maxima close to $c^* = 0$ and their minima near $c^* = 0.5$. To reach an optimum match, we have to add the two contributions and yield a predicted nesting vector of $q_{th} = 0.93a^* + 0.28c^*$, which is in excellent agreement with the observed value.

3.3.3 Superconductivity. As far as the superconducting properties of $ZrTe_3$ are concerned, the bands in the vicinity of B seem to be most relevant. Along the symmetry lines B–D and A–E the bands derived from the p_x orbitals of Te(2) and Te(3) exhibit only small dispersion and go through a saddle point at B with low Fermi velocity (blue region of the cylindric FS close to B in Fig. 7). A second saddle point is associated with a band with dominant p_y character of Te(1) [with minor p_y contributions from Te(2)/Te(3) and Zr d_{yz}]. This band has a positive slope along B–Γ and a negative slope along B–A. At B the slope of the band is close to zero, and the electron velocity is very low (localized states). This band leads to a dark blue region of the inner planar sheet close to B. In summary, the three steep bands that cross the Fermi level are dominated by Zr d_{y^2}, Te(1) p_y, and p_{σ^*} orbitals, whereas the flat bands in the vicinity of E_F have almost exclusively p_{σ^*} character. These findings may be related in a simple fashion

with a tendency to pairwise localization of the conduction electrons in the $p_{\sigma*}$ MOs of the Te_2 units.[28]

The special shape of the steep and flat bands is particularly interesting, as they give rise to saddle points in the vicinity of B. Saddle points at E_F[29] are known from the A15 compounds[30] and the layered high T_c oxocuprates.[31] An important finding with respect to the coexistence of a CDW and superconductivity in $ZrTe_3$ is that these physical phenomena may be related to different and independent features of the electronic band structure. In this context we point out that it is well known that a high DOS (E_F) can also induce structural instabilities. A static lattice distortion leads to electron localization, *i.e.* CDW and superconductivity are competing effects. A characteristic feature of the electronic band structure of a superconductor might be the simultaneous presence of wide and flat bands at E_F,[32] where the wide bands may take up delocalized electrons (as in a normal metal) and the narrow bands contain locally paired electrons. Within certain limits, this picture applies for $ZrTe_3$, and it has been put forward for a number of centered rare earth halide cluster compounds[33,34] and rare earth carbide borides.[35]

3.3.4 Frozen phonon calculations. Although we can rationalize the electronic properties of $ZrTe_3$ to some extent, there remain questions to be answered. From the above discussion it seems evident that the CDW is associated with the Fermi surface derived from bands of the linear chain of Te atoms [Te(2)/Te(3)]. The particular shape of these bands is related to 'soft bonds' between the Te atoms of adjacent trigonal prismatic units, and 'soft phonon modes' along the direction of the Te(2)—Te(3) vector will have a significant influence on the electronic structure of $ZrTe_3$. A lock-in of the CDW should have a pronounced effect on the Te(2)—Te(3) bond length and, correspondingly, should be associated with a q vector perpendicular to c^*, whereas an additional c^* component for q is observed experimentally. To get more information about the relationship between CDW and superconductivity, we have performed so-called frozen phonon calculations, where the electronic band structure is computed for a slightly distorted lattice; the static distortion provides a 'snapshot' of the dynamic atom displacement in the corresponding vibration mode. Fig. 8 shows that small changes in the atom positions lead to significant changes in the band structure, in particular the position of the Te p_σ and $p_{\sigma*}$ bands with respect to E_F. Within the local density approximation this calculation can only be performed for wave vectors at high symmetry points. We present only the results for Γ phonons, which means an identical displacement of all Te(2) and Te(3) atoms within the chains. In Fig. 8(a)–(d) we show the $ZrTe_3$ LMTO band structure where the Te(2)—Te(3) intra- and interprism distances were varied from the starting values of 2.72 Å and 3.20 Å in steps of 0.08 Å, *i.e.* Fig. 8(a) refers to a compressed Te(2)—Te(3) intraprism bond, Fig. 8(b) shows the bands for the experimental $ZrTe_3$ structure, Fig. 8(c) refers to a structure with partially equalized bond lengths and Fig. 8(d) refers to equidistant Te(2) and Te(3) atoms and a distance of 2.96 Å. The displacement vectors of the Te atoms in the CDW state are not known. We have not simulated a realistic incommensurable nesting vector. Nonetheless, we believe that a change in the Te(2)—Te(3) distances along a would play a major rôle in the nesting of the FS. This in turn would affect the Te p_σ band and the remaining three bands around the Fermi level. As expected, a compression of the intraprism Te(2)—Te(3) bond [Fig. 8(a)] leads to an increase of antibonding interactions. As a result, the $p_{\sigma*}$ band rises in energy, and only the flat regions (E–D–B–A) of the lower $p_{\sigma*}$ band are filled; the parallel sections of the FS vanish. The Te—Te chain is 'oxidized', *i.e.* electrons from Te(2) and Te(3) are transferred to the Zr d_{y^2} band, which cuts E_F along Γ–Z; as a result, an electron pocket develops around Z. The two saddle points close to B are still present, as the position of the associated band below E_F does not change significantly.[36] Further adjustment of the Te(2)—Te(3) distances shifts the $p_{\sigma*}$ band to lower energy, whereas the Zr d_{y^2} and the Te(1) p_y bands are pushed up [Fig. 8(c) and (d)] with respect to their positions for the experimental $ZrTe_3$ structure [Fig. 8(b)]. For a Te chain with equidistant Te atoms the Te(2)—Te(3) chain is 'reduced', *i.e.* the Te(2)/(3) $p_{\sigma*}$ band becomes filled; the Zr d_{y^2} band rises in energy and does not cross E_F (along Γ–Z), *i.e.* the metal is 'oxidized'. Similarly, the Te(1) centered p_y band rises in energy; it cuts E_F along Y–Γ, D–B, and B–A, and ends up above the Te $p_{\sigma*}$ at B. The most important changes in the band structure are observed at E and A, where the p_σ and $p_{\sigma*}$ bands of the one-dimensional Te—Te chain are degenerate. Even for equidistant Te(2) and Te(3) atoms, parallel sections of the Fermi surface are present as the degenerate p_σ and $p_{\sigma*}$ bands cross E_F along E–C and A–Y. In summary, the 'soft' Te_2 units form a charge reservoir which experiences a permanent dynamic change as a result of atom vibrations; in addition, the metal states are affected by changes in the Te(2)—Te(3) distances as well.

3.3.5 Comparison of the $ZrTe_3$, $HfTe_3$, and $ThTe_3$ band structures. In Fig. 9 we compare the band structures of the isostructural and isoelectronic $ZrTe_3$, $HfTe_3$[37] and $ThTe_3$.[38] In general, similarities can be expected; therefore we plot the bands only in the region close to E_F for these three compounds. The band structures of $ZrTe_3$ and $HfTe_3$ have very similar features; therefore similar electronic behavior may be expected for both compounds. In the band structures of both compounds the Te(2)/Te(3) p_x derived band intersects the Fermi level E_F along the C–E and A–Y directions. The resulting Fermi surface branch has a sheetlike shape parallel to the b^*, c^* plane close to the BZ boundary. Along Y to Γ not only the Te(1) p_y but

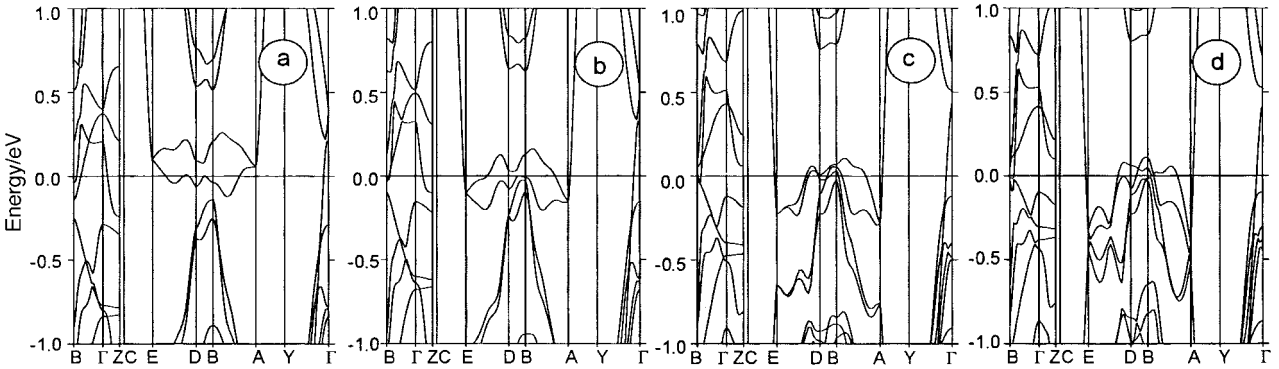

Fig. 8 'Frozen phonon' calculation. The results for a phonon wave vector $q=(0,0,0)=\Gamma$ are shown. The Te(2)—Te(3) distances within the trigonal $ZrTe_3$ prisms are (a) 2.72, (b) 2.80, (c) 2.88 and (d) 2.96 Å [3.20, 3.12, 3.04, and 2.96 Å for the corresponding Te(2)—Te(3) distances between adjacent prisms].

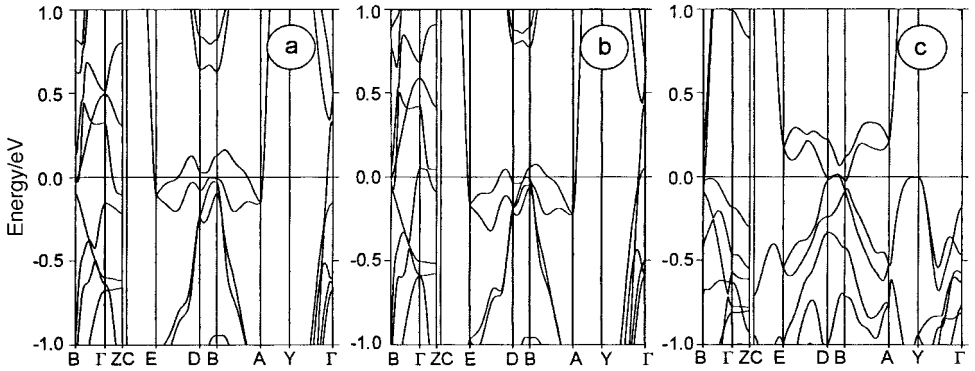

Fig. 9 Comparison of the TB-LMTO-ASA band structures of (a) $ZrTe_3$, (b) $HfTe_3$ and (c) $ThTe_3$

also the corresponding Te(1) p_x crosses E_F. This band intersects E_F again near Γ along Γ–B to drop below E_F again near Z with an avoided crossing of the metal d_{y^2} band. For $ThTe_3$ the situation is significantly different as now the Th d states appear at higher energy than the Zr d and the Hf d states. The p_x derived bands of the Te(2)/Te(3) chain that were situated at the Fermi level for $ZrTe_3$ and $HfTe_3$ are moved to higher energy now, and are almost completely unoccupied with a small hole pocket near B. The absence of parallel sections of the FS seems to be incompatible with the appearance of a CDW.

3.4 Physical measurements

3.4.1 Thermopower measurements. Fig. 10 shows the single crystal resistivities and Seebeck coefficients measured parallel to the crystallographic *a* and *b* axes. Above 75 K, the Seebeck coefficient *S* of $ZrTe_3$ is almost temperature independent with values along *a* and *b* of $S_a = (-12 \pm 1\ \mu V\ K^{-1}$ and $S_b = (+7 \pm 1)$ $\mu V\ K^{-1}$, in the same range as values of typical transition metals like Mo ($5.5\ \mu V\ K^{-1}$) or Pd ($-10\ \mu V\ K^{-1}$) at room temperature.[39] Below 75 K, S_a rapidly approaches zero and changes sign to positive values at 28 K. In contrast, S_b starts to increase at 75 K, reaches a broad maximum between 40 K and 50 K, and falls off rapidly below. The small hump around 250 K in both plots is an artefact from the experimental setup. Thermopower[39] is known to be very sensitive to the shape of the Fermi surface. It is generally discussed in terms of two contributions, the diffusion thermopower and the phonon drag. Although systems like $ZrTe_3$ are far too complicated for an accurate treatment, certain features of electronic structure can

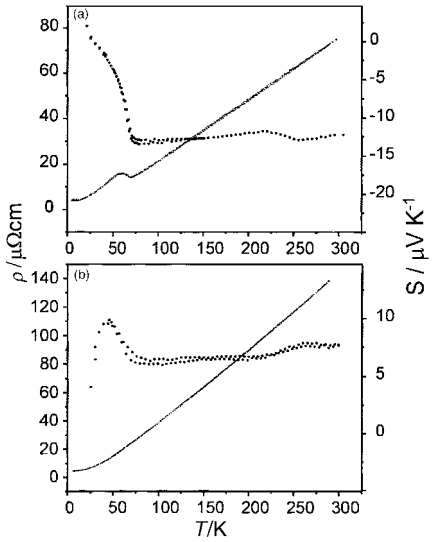

Fig. 10 Temperature dependent thermopower and resistivity measurements on a $ZrTe_3$ crystal (a) along the *a* axis, and (b) along the *b* axis

be satisfactorily matched with attributes of the thermopower plots. Electron transport along *a* is likely to be dominated by the second branch of the Fermi surface (Fig. 7), consisting of parallel planes perpendicular to the current flow. This feature is also responsible for the CDW nesting, and the drop in thermopower perfectly matches the onset of the CDW which causes the Fermi surface sheet to vanish. The corresponding bands are flat and the Fermi velocity is low, hence the diffusion term is expected to give a minor contribution to the total thermopower. For the phonon drag, we predict the dominant electron–phonon scattering to be an *Umklapp* (U) process, which can be viewed as scattering onto the FS sheet nearby in the repeated zone scheme. Since the zone filling is inverse to the situation in simple metals (*i.e.* the borders are filled), a U process gives rise to forward phonon drag scattering and a negative sign of thermopower, as found in the experiment. Generally, the phonon drag should diminish by $1/T$ at higher temperatures. However, no such temperature dependence is found. Interestingly, the thermopower along *b* is also affected by the CDW transition, although the transition vector is perpendicular to *b* and the parallel sheets cannot effect S_b. Since no resistivity anomaly is observed in this direction, the change is unlikely to be connected with the diffusion term (*i.e.* a change of the mean free path) and again the phonon drag is believed to be responsible. During the formation of the CDW, the thermopower almost doubles from 6 to 10 $\mu V\ K^{-1}$, indicating either a distinct change of the shape of the inner sheet of the Fermi surface, or of the phonon spectrum, or both. Our frozen phonon calculations provide some support for the first factor: it is not the top surface (Γ–Y direction) of the FS sheet, but its base area (spanned by B–Γ–Z) which changes dramatically upon changing the Te(2)—Te(3) distance. The drop in the magnitude of *S* below 40 K is probably due to 'freezing out' of phonons. The positive sign of S_b is in agreement with the hole-like character of the FS sheet close to the zone center, allowing mainly n-type scattering processes.

3.4.2 Photoemission. To obtain a more detailed idea of the electronic structure of $ZrTe_3$ we collected temperature dependent photoemission data using synchrotron radiation with excitation energies $h\nu = 70$, 100, 140 eV. An early photoemission study on $ZrTe_3$ was reported by Zhao *et al.*[40] in the low energy range between 16 and 24 eV. These spectra are thus complementary to results reported here. Fig. 11 shows the energy distribution curves (EDCs) recorded with photon energies of 70 eV (lower curve) and 100 eV (upper curve). To allow a comparison of the theoretical density of states with the spectral features we list in Table 1 the calculated cross sections[41] for the Zr s and d as well as for the Te s and p orbitals. The spectral data in Fig. 11 reveal a clear Fermi cutoff which reflects the metallic properties of the compound. In the EDC acquired at 70 eV excitation energy there are three spectral features, labeled A, E and F, with binding energies of 1.5, 4.7

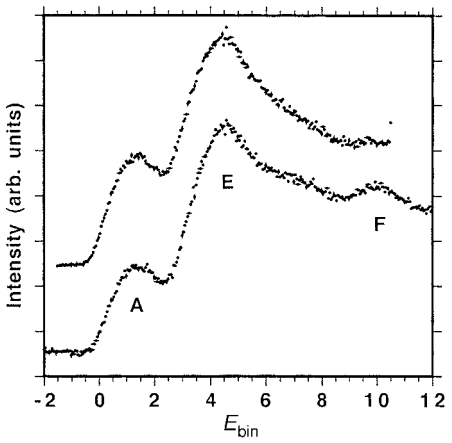

Fig. 11 Energy distribution curves (EDC) of $ZrTe_3$, with excitation energies of $hv = 70$ eV (upper trace) and 100 eV (lower trace)

Table 1 Photoemission cross sections relative to the zirconium 4d cross section, which is set to one (from ref. 41)

hv/eV	Zr 5s	Te 5s	Te 5p
20	0.3	0.0	3
70	0.8	0.3	20
100	0.5	2.0	12
140	0.5	0.8	6

and 10 eV. The peak at 10 eV was outside the energy range studied by Zhao *et al.* However, Zhao *et al.* observed an additional peak with a binding energy of 2.5 eV for lower excitation energies, which was not detected in our study. From our spectral data we derive a width of approximately 5.7 eV for the valence band, which is comparable with the value of 5.9 eV given by Zhao *et al.*[40]

The energy distribution curves in Fig. 11 are in excellent agreement with the computed density of states in Fig. 5. The Te s states are located at -10 eV whereas the valence band spreads out between -5.7 eV (width of the valence band) and the Fermi energy. The experimental DOS is dominated by the Te 5p and Zr 4d states, with pronounced peaks at -1.5 and -4.7 eV. The broad feature around -10 eV arises due to the s states of Te. To establish the orbital character of the features we combine knowledge of the band structure with the calculated subshell photoionization cross sections.[41] From the theoretical values in Table 1 it is apparent that the tellurium p states dominate all recorded spectra. However, an inspection of the cross section curve indicates that the Zr d states have a minimum cross section around 70 eV and are more dominant at low excitation energies. Furthermore, peak A has minimum intensity relative to peak E in the 70 eV spectrum and the spectrum reported by Zhao *et al.*, whereas peak C is not observed in our spectra. Therefore we assume that the peaks A and C with binding energies of 1.5 eV and 2.5 eV have substantial contributions from the Zr d orbitals.

The experimental data find support from the computed partial DOS for the Zr d states in Fig. 4(b). The contribution of the Zr d states to the valence band increases as we approach the Fermi energy, and the spectral features at -1.5 and -2.5 eV find a close match in the computed density of states. The previous discussion has shown that the states at E_F have $p_{\sigma*}$ character and are almost exclusively centered on Te(2) and Te(3). Furthermore, the states at -4.7 eV are associated with the p_x states of Te(2) and Te(3) at the bottom of the p_σ band. As can be seen from the DOS projections, the Te(1) contribution is small compared to the Te(2)/Te(3) contribution at the bottom of the valence band. In summary, the experimental and theoretical data are compatible. The excellent agreement between the computed DOS and the experimental data

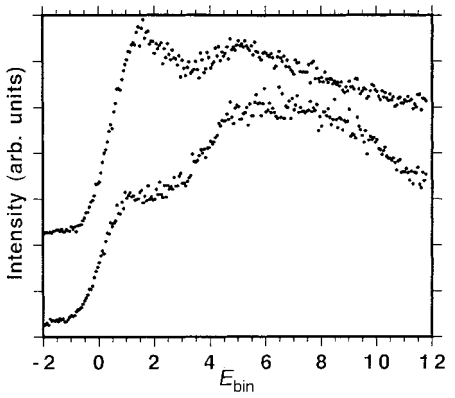

Fig. 12 Temperature dependent EDC at $T = 80$ K (upper trace) and 290 K (lower trace) with an excitation energy of $hv = 140$ eV

indicates that final states effects are irrelevant at the photon energies used. The temperature dependence of the spectral features may be understood in a qualitative fashion and give some additional information concerning the CDW in $ZrTe_3$. Fig. 12 displays the EDCs of $ZrTe_3$ acquired at an excitation energy of $hv = 140$ eV at two different temperatures, the upper curve corresponding to 80 K and the lower curve to 290 K. The most significant result is that close to the transition temperature the relative intensities of peaks A and E change. Photoemission from states slightly below E_F increases at the expense of the photoemission from the bottom of the valence band. If we compare this with the results of the frozen phonon calculations in Fig. 9, a change of the Te(2)—Te(3) distances affects the density of states around E_F significantly, through an enhancement of Te p states near E_F. This could be one of the two interpretations for the temperature dependence seen in the photoemission spectra. The other is that there is an increase in the population of Zr d states near the transition. The present data do not discriminate these two mechanisms adequately.

4 Conclusion

$ZrTe_3$ is a layer compound with a resistance anomaly at 63 K that has been attributed to the formation of a charge density wave and a transition to the superconducting state at below 2 K. $ZrTe_3$ is structurally related to the group 5 trichalcogenides, but its physical properties are very different from those of the group 5 congeners as the conductivity is perpendicular instead of parallel to the trigonal prism chains. We have related the physical properties of $ZrTe_3$ to its crystal and electronic structure and compared the band structure to the computed band structures of $HfTe_3$ and $ThTe_3$. In chemical terms, fractional 'soft' bonds between the Te atoms within and between the trigonal prismatic MTe_3 (M = Zr, Hf, Th) chains are responsible for a partial overlap between the chalcogen p-block bands and the metal d-block, *i.e.* the top of the Te band interpenetrates the bottom of the metal bands. As a result, there is a significant charge transfer from the Te atoms to the metal (and *vice versa*). The metallic behavior of $ZrTe_3$ may easily be understood based on this simple model. The bands in the vicinity of the Fermi level have mostly Te—Te $p_{\sigma*}$ bonding character, therefore very small changes in the Te—Te bonding can lead to large changes in the electronic structure and the physical properties. The computed Fermi surface of $ZrTe_3$ consists of three branches: two open and quasi-planar branches that are associated with the Te_2 groups, and an inner cylindrical section. The latter is responsible for the metallic properties. The observed CDW behavior can be related to the nesting of quasi-planar branches by a vector $q = 0.93a^* + 0.28c^*$. The special shape of the steep bands [with Zr d_{y^2}, Te(1) p_y and $p_{\sigma*}$] and flat $p_{\sigma*}$ bands in the vicinity of the

special point B give rise to saddle points at E_F that may be related to the superconducting properties of $ZrTe_3$. An important result with respect to the coexistence of a CDW and superconductivity in $ZrTe_3$ is that both phenomena can be related to different and independent features of the electronic band structure. Frozen phonon calculations which provide a snapshot of the dynamic atom displacements along a vibrational mode indicate that, similar to $NbSe_3$, the soft Te_2 units form a charge reservoir. This vibrational mode thus affects the FS significantly and would be strongly implicated in the phase transition. This would also mean that the electronic properties of $ZrTe_3$ are strongly pressure dependent. A comparison of the computed band structures of $ZrTe_3$, $HfTe_3$, and $ThTe_3$ indicates that the electronic properties of $HfTe_3$ should be similar to those of $ZrTe_3$. The smaller electronegativity of Th ensures that in $ThTe_3$, metal and Te states are better separated. This makes the occurrence of a CDW in this compound unlikely.

The theoretical results are backed by experimental studies. Temperature dependent single crystal conductivity and thermopower measurements were performed for $ZrTe_3$. $ZrTe_3$ exhibits a resistivity anomaly perpendicular to the trigonal prism chains; the single crystal Seebeck coefficients are consistent with the calculated Fermi surface. Photoemission spectra using synchrotron radiation with different excitation energies are in excellent agreement with the computed densities of states.

Support from the Deutsche Forschungsgemeinschaft and the Fonds der Chemischen Industrie is gratefully acknowledged. We thank E. Rochholz for help with the drawings, Dr. S. Cramm for his support during the photoemission measurements and Dr. R. Seshadri for a critical reading of the manuscript.

References

1 (*a*) F. K. McTaggart, *Aust. J. Chem*., 1958, **11**, 445; (*b*) W. Krönert and K. Plieth, *Z. Anorg. Allg. Chem*., 1965, **336**, 207; (*c*) L. Brattas and A. Kjekshus, *Acta Chem. Scand*., 1972, **26**, 3441; (*d*) S. Furuseth, L. Brattas and A. Kjekshus, *Acta Chem. Scand*., *Ser. A*, 1975, **29**, 623.

2 (*a*) D. W. Bullett, *Theoretical Aspects of Band Structures and Electronic Properties of Pseudo-One-Dimensional Solids*, ed. H. Kamimura, Reidel, Dordrecht, The Netherlands, 1985, p. 13; (*b*) S. Kurita, J. L. Straehli, M. Guzzi and F. Lévy, *Physica B*, 1981, **105**, 169; (*c*) J. A. Wilson, *Phys. Rev. B*, 1979, **19**, 6456; (*d*) F. S. Khumalo, C. G. Olson and D. W. Lynch, *Physica B*, 1981, **105**, 163; (*e*) H. G. Grimmeis, A. Rabenau, H. Hahn and P. Neiss, *Z. Elektrochem*., 1961, **65**, 776; (*f*) W. Schairer and M. W. Shafer, *Phys. Status Solidi A*, 1973, **17**, 181; (*g*) F. S. Khumala and H. P. Hughes, *Phys. Rev. B*, 1980, **4**, 2078; (*h*) G. Perluzzo, S. Jandl and P. E. Girard, *Can. J. Phys*., 1980, **58**, 143; (*i*) S. F. Nee, T. W. Nee, S. F. Fan and D. W. Lynch, *Phys. Status Solidi B*, 1982, **113**, K5; (*j*) H. W. Myron, B. N. Harmon and F. S. Khumalo, *J. Phys. Chem. Solids*, 1981, **42**, 263.

3 (*a*) S. Takahashi, T. Sambongi and S. Okada, *J. Phys.* (*Paris*) *Colloq*., 1983, **44**, C3–1733; (*b*) S. Takahashi, T. Sambongi, J. W. Brill and W. Roark, *Solid State Commun*., 1984, **49**, 1031.

4 (*a*) S. L. Herr and J. W. Brill, *Synth. Met*., 1986, **16**, 283; (*b*) S. C. Bayliss and W. Y. Liang, *J. Phys. C: Solid State Phys*., 1981, **14**, L803; (*c*) T. N. O'Neal, J. W. Brill, B. Ganguly, X. D. Xiang and G. Minton, *Synth. Met*., 1989, **31**, 215.

5 (*a*) A. Meerschaut and J. Rouxel, *J. Less-Common Met*., 1975, **39**, 498; (*b*) J. Chaussy, P. Haen, J. C. Lasjaunias, P. Monceau, G. Waysand, A. Waintal, A. Meerschaut, P. Molinie and J. Rouxel, *Solid State Commun*., 1976, **20**, 759; (*c*) P. Monceau, N. P. Ong, A. M. Portis, A. Meerschaut and J. Rouxel, *Phys. Rev. Lett*., 1976, **37**, 602.

6 J. A. Wilson, *Philos. Trans. R. Soc. A*, 1985, **314**, 159.

7 D. J. Eaglesham, J. W. Steeds and J. A. Wilson, *J. Phys. C*, 1984, **17**, 697.

8 H. Nakajima, K. Nomura and T. Sambongi, *Physica B*, 1986, **143**, 240.

9 E. Canadell, Y. Mathey and M.-H. Whangbo, *J. Am. Chem. Soc*., 1988, **110**, 104; a qualitative description of the bonding in $ZrTe_3$ has been given by W. Tremel and R. Hoffmann, *J. Am. Chem. Soc*., 1987, **109**, 124.

10 S. Furuseth and H. Fjellvag, *Acta Chem. Scand*., 1991, **45**, 694.

11 A. Briggs, P. Monceau, M. Munez-Reguero, J. Peyrard, M. Ribault and J. Richard, *J. Phys. C*, 1980, **36**, 983.

12 E. W. Finckh, C. Felser, G. Ouvrard and W. Tremel, *J. Alloys Compd*., 1997, **262–263**, 97.

13 (*a*) R. Schöllhorn, *Angew. Chem*., 1980, **92**, 1015; *Angew. Chem., Int. Ed. Engl*., 1980, **29**, 983; (*b*) R. H. Friend and A. D. Yoffe, *Adv. Phys*., 1987, **36**, 1.

14 (*a*) Extended Hückel approximation: R. Hoffmann, *J. Chem. Phys*., 1963, **39**, 1397; (*b*) weighted H_{ij} elements: J. H. Ammeter, H.-B. Bürgi, J. C. Thibeault and R. Hoffmann, *J. Am. Chem. Soc*., 1978, **100**, 3686; (*c*) tight-binding approximation: M.-H. Whangbo and R. Hoffmann, *J. Am. Chem. Soc*., 1978, **100**, 6093; M. H. Whangbo, R. Hoffmann and R. B. Woodward, *Proc. R. Soc. London A*, 1979, **366**, 23.

15 EHMACC program for extended Hückel molecular and crystal calculations: M.-H. Whangbo, M. Evain, T, Hughbanks, M. Kertesz, S. Wijesekera, C. Wilker, C. Zheng and R. Hoffmann; special k point set for average properties: R. Ramirez and M. C. Böhm, *Int. J. Quantum Chem*., 1986, **30**, 391.

16 U. von Barth and L. Hedin, *J. Phys. C*, 1972, **4**, 2064.

17 The lattice parameters expressed in cartesian coordinates were used, the primitive translation vectors are $t_1 = a\cos\beta\boldsymbol{i} + a\sin\beta\boldsymbol{j}$, $t_2 = b\boldsymbol{j}$, and $t_3 = c\boldsymbol{k}$. The special symmetry points are expressed by the primitive vectors of the reciprocal lattice in the following way: $g_1 = 2\pi/a[(1/\sin\beta)\boldsymbol{i}]$, $g_2 = 2\pi/b$, and $g_3 = 2\pi/c(\boldsymbol{k} - \cot\beta\boldsymbol{i})$.

18 O. K. Andersen, *Phys. Rev. B*, 1975, **12**, 3060.

19 H. L. Skriver, *The LMTO Method*, Springer, Berlin, 1984.

20 C. J. Bradley and A. P. Cracknell, *The Mathematical Theory of Symmetry in Solids*, Clarendon Press, Oxford, 1972.

21 G. Krier, O. Jepsen, A. Burkhardt and O. K. Andersen, Program TB-LMTO-ASA 4.7 (Tight Binding-Linear Muffin Tin Orbital-Atomic Sphere Approximation), Stuttgart, 1996.

22 O. Jepsen and O. K. Andersen, *Z. Phys. B*, 1995, **97**, 35.

23 F. Boucher, O. Jepsen and O. K. Andersen, unpublished research.

24 (*a*) S. Wijeyesekera and R. Hoffmann, *Organometallics*, 1984, **3**, 949; (*b*) J.-Y. Saillard and R. Hoffmann, *J. Am. Chem. Soc*., 1984, **106**, 2006.

25 J. K. Burdett, R. Hoffmann and R. C. Fay, *Inorg. Chem*., 1978, **17**, 2553.

26 The term redox competition was coined by Rouxel and coworkers; related ideas have been put forward by Hoffmann and Zheng for representatives of the $ThCr_2Si_2$ structure: (*a*) R. Hoffmann and C. Zheng, *J. Phys. Chem*., 1985, **89**, 4175; see also: R. Hoffmann, *Angew. Chem*., 1987, **99**, 871; *Angew. Chem., Int. Ed. Engl*., 1987, **26**, 846; R. Hoffmann, *Solids and Surfaces: A Chemist's View of Bonding in Extended Structures*, VCH Publishers, New York, 1988. In transition metal chalcogenides, these ideas have been discussed in: (*b*) J. Rouxel, *Chem. Eur. J*., 1996, **2**, 1053; (*c*) S. Jobic and J. Rouxel, *J. Alloys Compd*., 1992, **178**, 233; (*d*) S. Jobic, P. Deniard, R. Brec, J. Rouxel, A. Jouanneaux and A. Fitch, *Z. Anorg. Allg. Chem*., 1991, **598**, 199.

27 A. J. Berlinsky, *Rep. Prog. Phys*., 1979, **42**, 1243.

28 A. Simon, *Angew. Chem*., 1997, **109**, 1872; *Angew. Chem., Int. Ed. Engl*., 1997, **36**, 1788.

29 L. van Hove, *Phys. Rev*., 1953, **89**, 1189.

30 J. Labbe and J. Friedel, *J. Phys. (Paris)*, 1966, **27**, 153.

31 J. Labbe and J. Bok, *Europhys. Lett*., 1987, **3**, 1225.

32 J. Ranninger, J. M. Robin and M. Eschrig, *Phys. Rev. Lett*., 1995, **74**, 4027.

33 H. Mattausch and A. Simon, *Angew. Chem*., 1995, **107**, 1764; *Angew. Chem., Int. Ed. Engl*., 1995, **34**, 1633.

34 H. Mattausch, A. Simon and C. Felser, *J. Phys. Chem*., 1997, **109**, 1051.

35 (*a*) D. Johrendt, C. Felser, C. Huhnt, G. Michels, W. Schäfers and A. Mewis, *J. Solid State Chem*., 1997, **129**, 254; (*b*) H. Mattausch, A. Simon, C. Felser and R. Dronskowski, *Angew. Chem*., 1996, **108**, 1805; *Angew. Chem., Int. Ed. Engl*., 1996, **35**, 1685.

36 The presence of a 'soft' Te—Te bond indicates that physical properties of $ZrTe_3$ would be strongly pressure dependent. Therefore we have modeled the application of external pressure by a 1–3% reduction of the c and a axes. As expected, the p_{σ^*} band is strongly affected by an axis compression, and pushed above the Fermi level. The absence of any Fermi surface nesting indicates that the CDW is suppressed by hydrostatic pressure. These findings are in agreement with preliminary results of pressure dependent magnetic susceptibility measurements. In order to obtain accurate structural data as a basis for theoretical studies, pressure dependent neutron structure investigations are currently being done.

37 H. Kleinke, E. W. Finckh, C. Felser and W. Tremel, *Chem. Ber.*, in press.
38 (*a*) J. Graham and F. K. McTaggart, *Aust. J. Chem.*, 1960, **13**, 67; (*b*) F. Rocker and W. Tremel, unpublished results.
39 R. D. Barnard, *Thermoelectricity in Metals and Alloys*, Taylor & Francis, London, 1972.
40 T. X. Zhao, A. D. Katani, P. Perfetti, G. Margaritondo and F. Levy, *Nuovo Cimento*, 1982, **1**, 549.
41 J. J. Yeh and I. Lindau *Atomic Data and Nuclear Data Tables*, 1985, **32**, 1.

Paper 8/02948B; *Received* 21*st April*, 1998